nature photonics

ARTICLES

https://doi.org/10.1038/s41566-018-0105-8

Bright colloidal quantum dot light-emitting diodes enabled by efficient chlorination

Xiyan Li[1,5], Yong-Biao Zhao[1,2,5], Fengjia Fan[1,3*], Larissa Levina[1], Min Liu[1,4], Rafael Quintero-Bermudez[1], Xiwen Gong[1], Li Na Quan[1], James Zhangming Fan[1], Zhenyu Yang[1], Sjoerd Hoogland[1], Oleksandr Voznyy[1*], Zheng-Hong Lu[2*] and Edward H. Sargent[1*]

The external quantum efficiencies of state-of-the-art colloidal quantum dot light-emitting diodes (QLEDs) are now approaching the limit set by the out-coupling efficiency. However, the brightness of these devices is constrained by the use of poorly conducting emitting layers, a consequence of the present-day reliance on long-chain organic capping ligands. Here, we report how conductive and passivating halides can be implemented in Zn chalcogenide-shelled colloidal quantum dots to enable high-brightness green QLEDs. We use a surface management reagent, thionyl chloride ($SOCl_2$), to chlorinate the carboxylic group of oleic acid and graft the surfaces of the colloidal quantum dots with passivating chloride anions. This results in devices with an improved mobility that retain high external quantum efficiencies in the high-injection-current region and also feature a reduced turn-on voltage of 2.5 V. The treated QLEDs operate with a brightness of 460,000 cd m^{-2}, significantly exceeding that of all previously reported solution-processed LEDs.

Light-emitting diodes (LEDs) provide superior contrast over liquid-crystal displays (LCDs) that rely on backlit panels. LEDs that are based on colloidal quantum dots (CQDs), QLEDs, provide improved colour purity and wavelength tunability compared with organic LEDs[1,2]. For these reasons, continuous efforts have been devoted to improving QLED performance towards the goal of enhanced display and lighting solutions[3–8].

Impressive peak external quantum efficiencies (EQEs) of 12%[9], 16.5%[10] and 20%[4] have been achieved in blue, green and red QLEDs, respectively. Instead of employing a single CQD monolayer[11], most recent architectures employ several dot layers, with the dots capped using organic ligands that reduce current leakage and suppress exciton quenching at the interfaces with charge transfer layers. These organic ligands also provide excellent passivation for high EQEs at low currents; however, because of the ligands' insulating nature, the EQE typically deteriorates at higher brightness[4,12,13]. Replacing long insulating organic ligands with conductive, passivating inorganic ligands has long been pursued to increase charge carrier mobility. This has worked well in the adjacent fields of CQD photovoltaics and field-effect transistor devices[14], with advances coming from halides[15,16], pseudo-halides[17] and metal complexes[18].

To fabricate efficient and bright QLEDs, it is imperative to combine excellent transport with optimized excitonic confinement[19,20]. This can be achieved by growing a passivating and confining shell that prevents exciton dissociation in conductive CQD solids and maintains efficient radiative recombination. The ZnS shell provides symmetric conduction and valence band offsets for the CdSe core, better confining the excitons and balancing the electron and hole mobilities[10,21].

However, a complete exchange with short, transport-compatible inorganic ligands, without compromising the quantum efficiency, has yet to be developed for ZnS-shelled CQDs[22–27]. Previously explored ligand exchange approaches have employed anion replacement reactions (Fig. 1)[17,18,28]. The driving force of this class of reaction arises from the difference in ligand binding energies before and after the exchange and is therefore significantly determined by the composition of the surface of the CQD[18]. Because of the distinct surface chemistry and large size of ZnS-shelled CQDs, it is challenging to implement ligand exchange through the anion replacement strategy.

For these reasons, QLEDs with simultaneously conductive and bright emitting layers have yet to be demonstrated. Here we developed a robust place exchange strategy, one that instead employs a chlorination reagent ($SOCl_2$, Fig. 1), that chlorinates and removes oleic acid ligands and then grafts conductive chloride ligands onto the CQD surface. The driving force for the chlorination reaction, which originates from the capacity of $SOCl_2$ to react with the carboxylic group of oleic acid, is sufficient to exchange ZnS-shelled CQDs and retain the desired excitonic confinement.

The ligand exchange thereby facilitates charge carrier transport, balancing the spatial distribution of electrons and holes, and thus reducing Auger recombination losses. The photoluminescence quantum yield (PLQY) of the resulting films remains high thanks to the sufficient retention of excitonic confinement.

Results and discussion

Material synthesis and photophysical properties. To achieve efficient QLEDs, we first sought to maximize the PLQY value in CQD solid films. We tested two kinds of CQDs with type I excitonic confinement: gradient-alloyed CdSeZnS core–shell (C–S) and CdSeZnS–ZnS core–shell–shell (C–S–S) CQDs. The double-shelled CQDs are obtained by growing an additional ZnS shell on the first

[1]Department of Electrical and Computer Engineering, University of Toronto, Toronto, Ontario, Canada. [2]Department of Materials Science and Engineering, University of Toronto, Toronto, Ontario, Canada. [3]Present address: CAS Key Laboratory of Microscale Magnetic Resonance and Department of Modern Physics, University of Science and Technology of China (USTC), Hefei, China. [4]Present address: Institute of Super-microstructure and Ultrafast Process in Advanced Materials, School of Physics and Electronics, Central South University, Changsha, China. [5]These authors contributed equally: Xiyan Li and Yong-Biao Zhao. *e-mail: ffj@ustc.edu.cn; o.voznyy@utoronto.ca; zhenghong.lu@utoronto.ca; ted.sargent@utoronto.ca

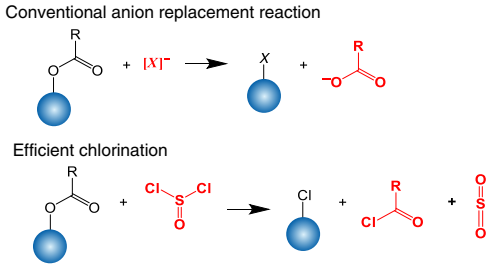

Fig. 1 | Chlorination ligand exchange mechanism. Chemical equations for conventional anion replacement (top) and efficient chlorination processes (bottom). *X* represents halides, pseudo-halides, sulfides, metal complexes and so on. Blue spheres and R denote CQD and aliphatic hydrocarbon groups, respectively. The red text highlights the major difference between the two reactions.

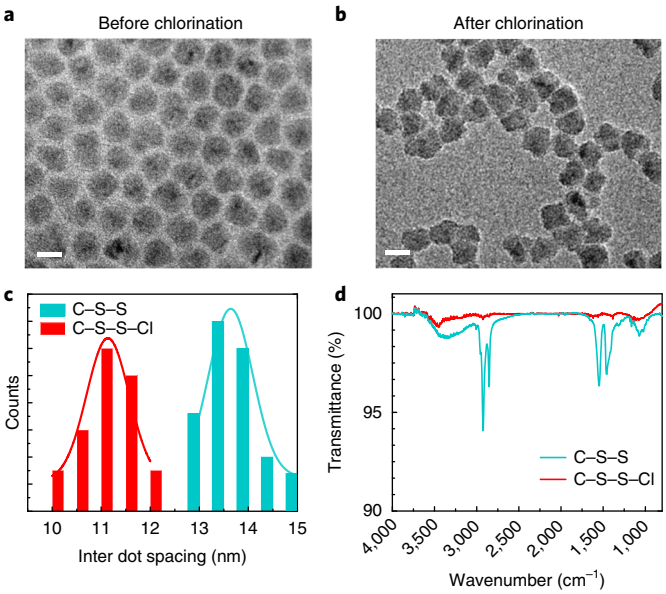

Fig. 2 | Characterization of C–S–S–Cl CQDs. a,**b**, TEM images of C–S–S (**a**) and C–S–S–Cl (**b**) CQDs. Scale bars, 10 nm. **c**, Histograms of the interdot spacings extracted from **a** and **b**. **d**, FTIR spectra of CQD films showing the removal of organic ligands following efficient chlorination.

shell (see Methods for synthesis details)[29,30]. The sizes of the C–S and C–S–S CQDs, measured using transmission electron microscopy (TEM) images, are 6 nm and 12 nm, respectively, indicating a ZnS shell thickness of 3 nm (Fig. 2a and Supplementary Fig. 1a). The blueshift of PL peak (514 nm, Supplementary Fig. 2) indicates a degree of interfacial alloying. The reduced linewidth (full width at half maximum (FWHM) 26 nm) reveals that the alloying process introduced a composition gradient that decreases the inhomogeneity among CQDs.

The PLQY of the C–S–S CQD solution (75%) is not dramatically different from that of the C–S CQD solution (70%), consistent with the slightly longer PL lifetime (21 ns versus 17 ns) (Supplementary Fig. 3). However, the difference in PLQY is increased when these same CQDs are deposited onto glass substrates. The dramatic drop in PLQY (from 70% to 45%) and shortening in PL decay lifetime in C–S CQD films are attributed to exciton dissociation and trap recombination assisted by Förster resonance energy transfer (FRET) (Supplementary Fig. 4, Supplementary Table 1)[21,31]. The extra ZnS shell reduces exciton migration and mitigates PL quenching, preserving high PLQY (63%) and long PL decay lifetime in films (Supplementary Fig. 5).

Efficient chlorination of CQD films. Next we sought to improve the conductivity of the C–S–S CQD films by replacing the insulating long-chain organic ligands with short and conductive halides[32]. Published solution–phase inorganic ligand exchanges[17] failed to provide stable colloids for ZnS-shelled CQDs, we ascribe this to strong binding betwen Zn and oleic acid and the large CQD size after shelling (Supplementary Fig. 6). We therefore focused on developing a solid-state in-place exchange, an approach that provides increased flexibility in the choice of reactive species for ligand exchange. However, we found that a conventional approach based on quaternary ammonium halides could not quantitatively remove the organic ligands[16,33,34]. Following exchange, the CQD films remained soluble in nonpolar solvents, and a strong C–H signal from oleic acid was detected (Supplementary Fig. 7). Chlorotrimethylsilane and propyltrichlorosilane were recently introduced as alternative treatments that are capable of replacing the organic ligands on the surface of CdSe-based dots with chloride anions[22,23]. However, in earlier publications, these exchanges greatly quenched the PL in solid films. This may be due to excessive shell etching caused by hydrogen chloride (a product of reaction between chlorolsilanes and trace amounts of moisture[35]), precluding their use in QLEDs.

We reasoned that a more efficient chlorination reagent that is widely used in organic synthetic chemistry, $SOCl_2$[35,36], which is compact in size and capable of reacting with the carboxylic group of oleic acid, could readily penetrate through the films and potentially remove oleic acid even if applied at low concentration. The concentration (0.014 M, see the Supplementary Information) was much lower than that required of tetrabutylammonium chloride (0.14 M, Supplementary Figs. 6,7)[17] and propyltrichlorosilane (0.5 M) used in previous reports[23]. This would reduce the generation of hydrogen chloride and circumvent excessive etching of the shell (see Methods for experimental details). This reaction yields CQDs that are passivated by chloride anions, and free acyl chloride and sulfur dioxide (Fig. 1), which are readily removed during the subsequent washing step.

TEM images of the C–S–S CQDs after efficient chlorination, hereafter referred to as C–S–S–Cl (Fig. 2b), reveal that the interdot distance is shortened after the chlorination (from ~13.5 nm to ~11 nm, Fig. 2c). This agrees well with the Fourier-transform infrared spectroscopy (FTIR) spectra (Fig. 2d). The characteristic signals attributed to oleic acid, that is, C–H_x stretching signals at 2,922 cm^{-1} and 2,852 cm^{-1}, and O=CO– vibrations at 1,545 cm^{-1} and 1,403 cm^{-1} are eliminated in exchanged films[23]. X-ray photoelectron spectra (Supplementary Fig. 8) further confirm that the CQD surface is grafted with chloride atomic ligands (Cl 2*p*, 199.5 eV) whereas the carboxyl groups (C 1*s*, at 289.2 eV) are removed[37], supporting the reaction scheme presented in Fig. 1.

More importantly, the PLQY is maintained (60 ± 2%) after chlorination and no redshift in PL wavelength is observed (Supplementary Fig. 9a), indicating that the excitons remain well confined. Furthermore, the PL decay dynamics of C–S–S–Cl CQDs remain unchanged when the ZnO/ITO substrate is used in place of glass (Supplementary Fig. 5), showing that CQDs do not become charged[38]. In contrast, even in C–S CQD films on a glass substrate, a significant PLQY decrease (from 45% to 30%) accompanied by a 6 nm redshift is observed following chlorination exchange (Supplementary Fig. 9b, Supplementary Table 1). This suggests that FRET-assisted trapping and exciton dissociation become more severe after the exchange.

Device fabrication and characterization. To ascertain whether these bright C–S–S–Cl films show improved transport properties, we fabricated devices with electron-only and hole-only injection,

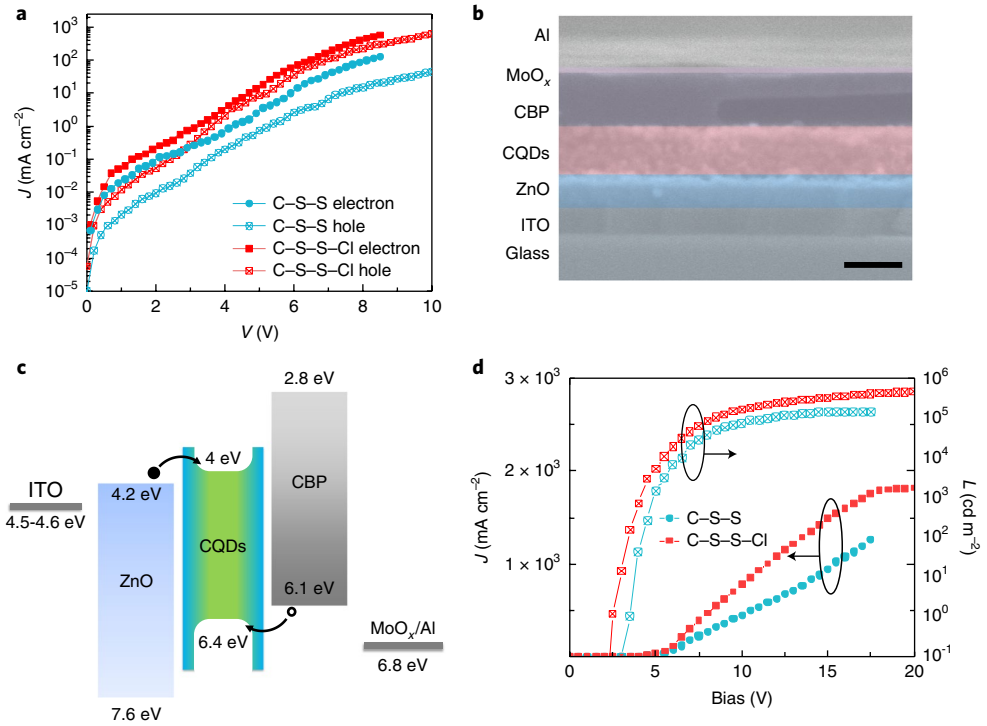

Fig. 3 | Conductivity and QLED architecture characterization. a, *J*–*V* characteristics of electron- and hole-only devices based on C-S-S and C-S-S-Cl CQDs. **b**,**c**, Cross-sectional SEM image (**b**; scale bar: 60 nm) and energy diagram (**c**) of the different layers of C-S-S-Cl QLEDs. **d**, *J*-*L*-*V* characteristics of the C-S-S and C-S-S-Cl QLEDs, respectively.

allowing us to measure current density–bias (*J*–*V*) characteristics (Fig. 3a) for each type of carrier independently. After chlorination-based place-exchange, both the electron and hole currents increased. By fitting the *J*–*V* curve using a space–charge limited current (SCLC) model (Supplementary Figs. 10–12)[39], we further confirmed that the mobility in the C–S–S–Cl film also increased (Supplementary Table 2, see fitting details in the Supplementary Information). Electron and hole currents are more balanced at high bias in both devices (Fig. 3a), as was also observed in previous reports[9,10,25]. We propose that the hopping transport mobility in disordered semiconductors depends strongly on injection level[40] because the density of transport-associated states varies with depth relative to the bandedge[41]. In the case of CQDs, this site energy disorder is dominated by CQD size dispersity; moreover, the conduction band and valence band dispersions are not necessarily the same[42] resulting in unbalanced mobilities at low injection levels. This disorder-induced imbalance can be suppressed at high bias as electron and hole mobilities are each enhanced to a different extent.

Encouraged by the above results, we fabricated C–S–S and C–S–S–Cl CQD-based QLEDs using an inverted device structure[43]. The cross-sectional SEM image, together with the energy diagram of different layers of the C–S–S–Cl QLED, is illustrated in Fig. 3b,c. Solution-processed ZnO nanoparticles (35 nm, Supplementary Fig. 13) and thermally evaporated 4,4′-bis(N-carbazolyl)-1,1′-biphenyl (CBP, 55 nm) were used as electron- and hole-transporting layers (ETL and HTL, the electron affinity and ionization potential were obtained according to published methods[44,45]), respectively. The thickness of the emissive CQD layer was 45–50 nm (4–5 layers of QDs). Atomic force microscope (AFM) images confirm that all the layers were pinhole free (Supplementary Figs. 13,14), and the root mean squared roughness of the C–S–S–Cl layer on ZnO film is 3.2 nm, which is slightly higher than that of the C–S–S layer (2.2 nm, see the Supplementary Information for ultraviolet photoelectron spectroscopy (UPS) data (Supplementary Figs. 15,16)).

The chloride exchange results in a substantial performance improvement over the pristine C–S–S CQD devices. As a result

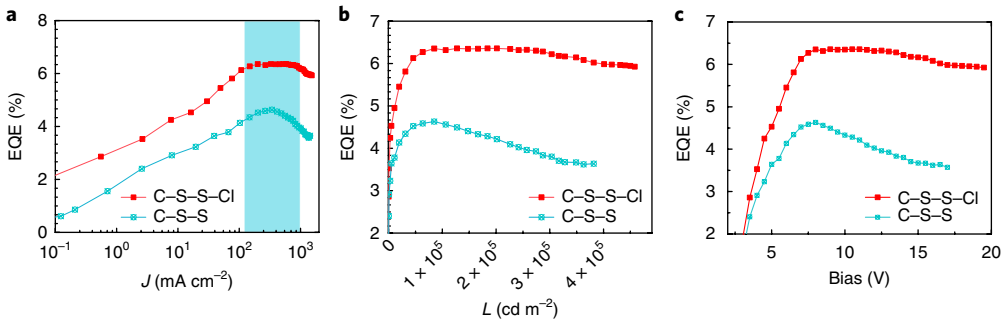

Fig. 4 | EQE characterization of QLED devices. a–**c**, EQE as a function of the current density (**a**), luminance (**b**) and bias (**c**) of the C-S-S and C-S-S-Cl QLEDs, respectively. The blue shaded bar in **a** highlights the EQE roll-off current densities.

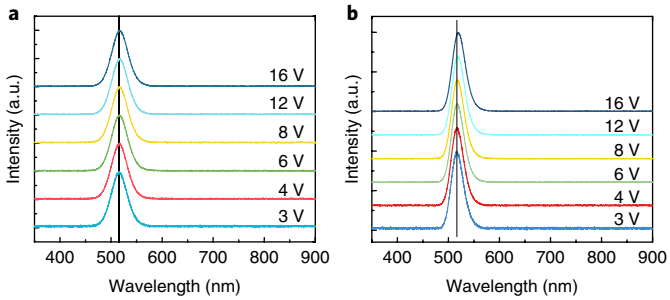

Fig. 5 | Electroluminescence spectra under different biases. a, C-S-S-Cl QLED devices. **b**, C-S-S QLED devices.

of the improved mobility, the C–S–S–Cl QLED shows higher current densities at given biases throughout the range measured. The turn-on voltage—defined where the brightness reaches 1 cd m^{-2}—is decreased from 3.5 V to 2.5 V (Fig. 3d, Supplementary Table 3). The turn-on voltage of the control device is lower than the value reported recently (~5.2 V) using similar C–S–S CQDs, indicating that the control devices are properly optimized[21]. The driving bias to achieve a benchmark luminance (L) of 1,000 cd m^{-2} was also reduced from 4.9 V to 3.9 V. The lowering in bias is helpful to mitigate the quantum-confined Stark effect, a fact that also contributes to the higher EQE in C–S–S–Cl devices at a given brightness[2].

We observed that the EQE increases with increasing the bias up to 7.5 V in both devices, as observed in previous reports[7,21,27]. This can be qualitatively understood by considering recombination $R(n)$ in QLEDs, which consists of three components: trap-assisted non-radiative Shockley–Read–Hall (An), radiative (Bn^2) and Auger (Cn^3) recombination (where A, B and C are the related coefficients)[46]. These components show linear, quadratic and cubic dependence on the carrier concentration n (equation (1)), respectively. As a result, recombination at the lowest bias is dominated by trap state recombination, at a medium bias by radiative recombination, and at a high bias by Auger recombination:

$$R(n) = An + Bn^2 + Cn^3 \quad (1)$$

To achieve high brightness, it is essential to maintain a high EQE at even higher bias and therefore higher current density. Similar to typical QLED devices reported previously, EQE roll-off becomes significant in the C–S–S QLED as the injected current density exceeds 350 mA cm^{-2} (Fig. 4a). In contrast, there is no obvious EQE roll-off up to 1,000 mA cm^{-2} in the C–S–S–Cl QLEDs (Fig. 4a). Similarly, the EQE starts to roll off at 85,000 cd m^{-2} in the C–S–S QLED, but remains nearly constant in the C–S–S–Cl QLED up to its maximum luminance of 460,000 cd m^{-2} (Fig. 4b).

In earlier reports, EQE roll-off has been attributed to three possible causes: Joule heating, the quantum-confined Stark effect[2,14] and Auger recombination[47]. We observed a slight redshift in the electroluminescence peak in C–S–S devices at a bias of 16 V (Fig. 5b), whereas it is less obvious in C–S–S–Cl devices (Fig. 5a), indicating that reduced Joule heating in Cl^- passivated devices may contribute to the improved maximum brightness. The quantum-confined Stark effect was excluded as the main cause since EQE roll-off in

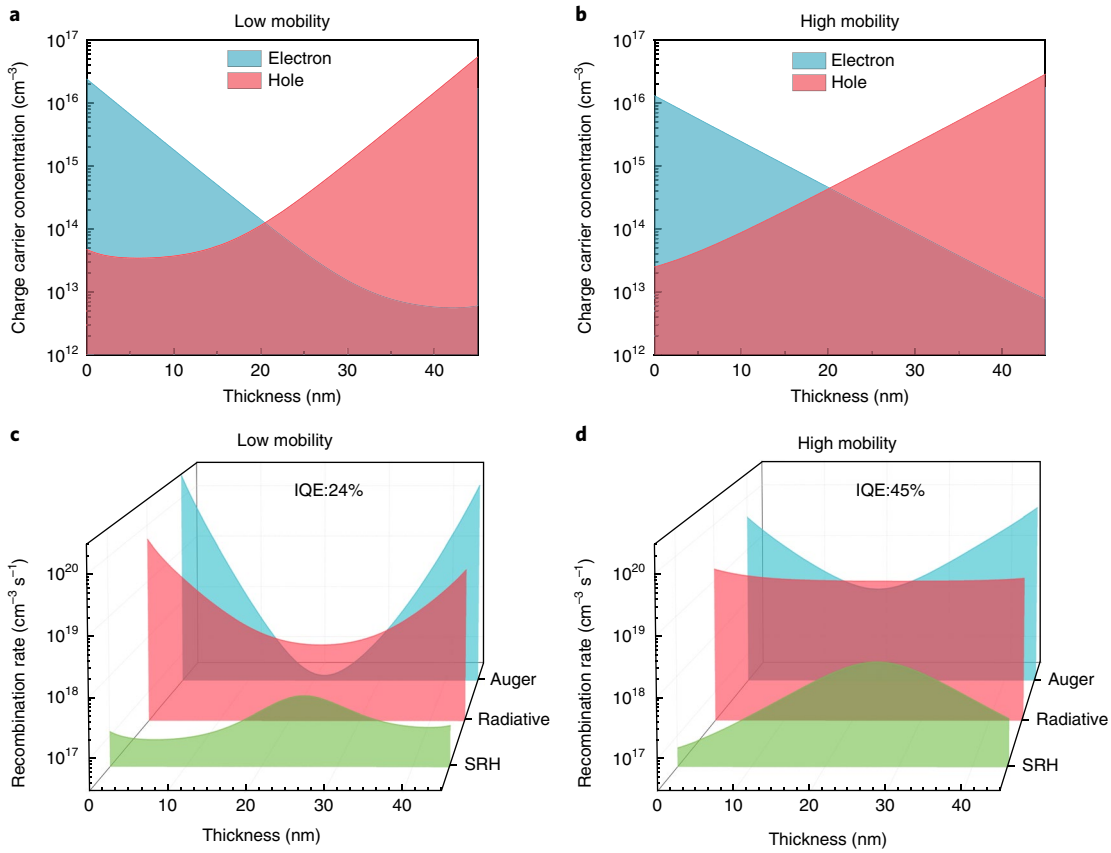

Fig. 6 | Optoelectronic simulations of charge carrier distributions and recombination rates inside the active layers. a,**b**, The charge carrier distribution inside the 45-nm-thick CQD active layers with low (**a**) and high (**b**) mobilities, respectively, at an equivalent injection current in a QLED. **c**,**d**, The corresponding recombination rates and the resultant IQE values (note the logarithmic scale). SRH, Shockley–Read–Hall recombination through trap states.

C–S–S–Cl QLEDs takes place at a much higher bias than in the control devices with identical confining potentials within each CQD (Fig. 4c). We therefore conclude that the reduced Auger recombination—its ratio lowered due to the increased mobility and a more balanced injection in the new devices—is the main cause of the reduced EQE roll-off in C–S–S–Cl devices.

Device modelling. This hypothesis is supported by more detailed optoelectronic device modelling (Fig. 6). A positive effect of increased mobility on reducing Auger recombination losses (see Methods for simulation details) is observed. Simulation results indicate that due to relatively high injection barriers (0.2–0.3 eV), electron and hole concentrations are depleted near the ETL and HTL, respectively, and accumulate at the opposite side of the device (Fig. 6a,b, and Fig. 3c). An improvement in mobility by an order of magnitude results in a more balanced distribution of electrons and holes throughout the thickness of the active layer (Fig. 6b). In the low-conductivity case, most charge carriers recombine near the edges, with a major portion lost through Auger recombination. In contrast, with higher mobility, radiative recombination occurs throughout the entire thickness of the layer. Higher mobility leads to a slightly increased trap recombination (Shockley–Read–Hall recombination in the plot), as this can now compete more efficiently with radiative recombination. The radiative-to-Auger recombination ratio has been improved so that a higher internal quantum efficiency (IQE) (Fig. 6c,d) can be obtained.

In our C–S–S–Cl device, an EQE of ~6% was obtained at a high current injection current density of 1,000 mA cm^{-2}, providing improved high-current performance compared with the best-reported QLEDs (Fig. 4a, Supplementary Table 4). As a result, a maximum brightness of 460,000 cd m^{-2} is demonstrated in C–S–S–Cl QLEDs (Fig. 3d). This is the highest value reported in an LED that employs solution-processed emitting layers (Supplementary Tables 4 and 5)[43,48].

Conclusion

We developed an efficient chlorination process that efficiently replaces organic ligands with inorganic single-atomic-layer surface ligands. When we combine efficient chlorination with judiciously engineered excitonic confinement, we obtained CQD films with simultaneously high conductivity and high quantum efficiency. This facilitates charge carrier injection and mitigates the accumulation of electrons and holes near the ETL and HTL. Auger recombination was therefore suppressed at high injection current densities. As a result, the turn-on voltage of chlorinated QLEDs was reduced from 3.5 V to 2.5 V, and the roll-off current threshold was increased, resulting in a maximum brightness of 460,000 cd m^{-2}—a value two times higher than previously reported LEDs that employ solution-processed emitting layers. This strategy can be extended to QLEDs with different emission wavelengths to mitigate efficiency roll-off at high injection current densities and enable light sources with high brightness. It also represents a step towards electrically pumped CQD lasers[49].

Methods

Methods, including statements of data availability and any associated accession codes and references, are available at https://doi.org/10.1038/s41566-018-0105-8.

Received: 30 May 2017; Accepted: 17 January 2018;
Published online: 26 February 2018

References

1. Reineke, S. Complementary LED technologies. *Nat. Mater.* **14**, 459–462 (2015).
2. Shirasaki, Y., Supran, G. J., Bawendi, M. G. & Bulović, V. Emergence of colloidal quantum-dot light-emitting technologies. *Nat. Photon.* **7**, 13–23 (2013).
3. Colvin, V. L., Schlamp, M. C. & Alivisatos, A. P. Light-emitting-diodes made from cadmium selenide nanocrystals and a semiconducting polymer. *Nature* **370**, 354–357 (1994).
4. Dai, X. et al. Solution-processed, high-performance light-emitting diodes based on quantum dots. *Nature* **515**, 96–99 (2014).
5. Cho, K.-S. et al. High-performance crosslinked colloidal quantum-dot light-emitting diodes. *Nat. Photon.* **3**, 341–345 (2009).
6. Qian, L., Zheng, Y., Xue, J. & Holloway, P. H. Stable and efficient quantum-dot light-emitting diodes based on solution-processed multilayer structures. *Nat. Photon.* **5**, 543–548 (2011).
7. Mashford, B. S. et al. High-efficiency quantum-dot light-emitting devices with enhanced charge injection. *Nat. Photon.* **7**, 407–412 (2013).
8. Dai, X., Deng, Y., Peng, X. & Jin, Y. Quantum-dot light-emitting diodes for large-area displays: towards the dawn of commercialization. *Adv. Mater.* **29**, 1607022 (2017).
9. Shen, H. et al. High-efficiency, low turn-on voltage blue-violet quantum-dot-based light-emitting diodes. *Nano Lett.* **15**, 1211–1216 (2015).
10. Li, Z. et al. Efficient and long-life green light-emitting diodes comprising tridentate thiol capped quantum dots. *Laser Photon. Rev.* **11**, 1600227 (2017).
11. Coe, S., Woo, W.-K., Bawendi, M. & Bulović, V. Electroluminescence from single monolayers of nanocrystals in molecular organic devices. *Nature* **420**, 800–803 (2002).
12. Yang, Y. et al. High-efficiency light-emitting devices based on quantum dots with tailored nanostructures. *Nat. Photon.* **9**, 259–266 (2015).
13. Shirasaki, Y., Supran, G. J., Tisdale, W. A. & Bulović, V. Origin of efficiency roll-off in colloidal quantum-dot light-emitting diodes. *Phys. Rev. Lett.* **110**, 217403 (2013).
14. Dolzhnikov, D. S. et al. Composition-matched molecular "solders" for semiconductors. *Science* **347**, 425–428 (2015).
15. Tang, J. et al. Colloidal-quantum-dot photovoltaics using atomic-ligand passivation. *Nat. Mater.* **10**, 765–771 (2011).
16. Chuang, C.-H. M., Brown, P. R., Bulović, V. & Bawendi, M. G. Improved performance and stability in quantum dot solar cells through band alignment engineering. *Nat. Mater.* **13**, 796–801 (2014).
17. Zhang, H., Jang, J., Liu, W. & Talapin, D. V. Colloidal nanocrystals with inorganic halide, pseudohalide, and halometallate ligands. *ACS Nano* **8**, 7359–7369 (2014).
18. Kovalenko, M. V., Scheele, M. & Talapin, D. V. Colloidal nanocrystals with molecular metal chalcogenide surface ligands. *Science* **324**, 1417–1420 (2009).
19. Choi, J. J. et al. Photogenerated exciton dissociation in highly coupled lead salt nanocrystal assemblies. *Nano Lett.* **10**, 1805–1811 (2010).
20. Sun, L. F. et al. Bright infrared quantum-dot light-emitting diodes through inter-dot spacing control. *Nat. Nanotech.* **7**, 369–373 (2012).
21. Lee, K.-H. et al. Over 40 cd/A efficient green quantum dot electroluminescent device comprising uniquely large-sized quantum dots. *ACS Nano* **8**, 4893–4901 (2014).
22. Owen, J. S., Park, J., Trudeau, P.-E. & Alivisatos, A. P. Reaction chemistry and ligand exchange at cadmium−selenide nanocrystal surfaces. *J. Am. Chem. Soc.* **130**, 12279–12281 (2008).
23. Zanella, M. et al. Atomic ligand passivation of colloidal nanocrystal films via their reaction with propyltrichlorosilane. *Chem. Mater.* **25**, 1423–1429 (2013).
24. Ji, C. et al. 1,2-Ethanedithiol treatment for $AgIn_5S_8$/ZnS quantum dot light-emitting diodes with high brightness. *ACS Appl. Mater. Inter.* **9**, 8187–8193 (2017).
25. Daekyoung, K. et al. Improved electroluminescence of quantum dot light-emitting diodes enabled by a partial ligand exchange with benzenethiol. *Nanotechnology* **27**, 245203 (2016).
26. Pan, J. et al. Highly efficient perovskite-quantum-dot light-emitting diodes by surface engineering. *Adv. Mater.* **28**, 8718–8725 (2016).
27. Yang, Z. et al. All-quantum-dot infrared light-emitting diodes. *ACS Nano* **9**, 12327–12333 (2015).
28. Dirin, D. N. et al. Lead halide perovskites and other metal halide complexes as inorganic capping ligands for colloidal nanocrystals. *J. Am. Chem. Soc.* **136**, 6550–6553 (2014).
29. Bae, W. K. et al. Highly efficient green-light-emitting diodes based on CdSe@ZnS quantum dots with a chemical-composition gradient. *Adv. Mater.* **21**, 1690–1694 (2009).
30. Bae, W. K., Nam, M. K., Char, K. & Lee, S. Gram-scale one-pot synthesis of highly luminescent blue emitting $Cd_{1-x}Zn_xS$/ZnS nanocrystals. *Chem. Mater.* **20**, 5307–5313 (2008).
31. Lim, J. et al. Influence of shell thickness on the performance of light-emitting devices based on CdSe/$Zn_{1-x}Cd_xS$ core/shell heterostructured quantum dots. *Adv. Mater.* **26**, 8034–8040 (2014).
32. Adachi, M. M. et al. Microsecond-sustained lasing from colloidal quantum dot solids. *Nat. Commun.* **6**, 8694 (2015).
33. Lan, X. et al. Passivation using molecular halides increases quantum dot solar cell performance. *Adv. Mater.* **28**, 299–304 (2016).
34. Ning, Z. et al. Air-stable n-type colloidal quantum dot solids. *Nat. Mater.* **13**, 822–828 (2014).

35. Di Raddo, P. A convenient method of esterification of fatty acids: An undergraduate organic laboratory experiment. *J. Chem. Educ.* **70**, 1034 (1993).
36. Montalbetti, C. A. & Falque, V. Amide bond formation and peptide coupling. *Tetrahedron* **61**, 10827–10852 (2005).
37. Bae, W. K. et al. Highly effective surface passivation of PbSe quantum dots through reaction with molecular chlorine. *J. Am. Chem. Soc.* **134**, 20160–20168 (2012).
38. Bae, W. K. et al. Controlling the influence of Auger recombination on the performance of quantum-dot light-emitting diodes. *Nat. Commun.* **4**, 2661 (2013).
39. Blakesley, J. C. et al. Towards reliable charge-mobility benchmark measurements for organic semiconductors. *Org. Electron.* **15**, 1263–1272 (2014).
40. Baranovski, S. *Charge Transport in Disordered Solids with Applications in Electronics* Vol. 17 (John Wiley & Sons, Chichester, 2006).
41. Talgorn, E. et al. Unity quantum yield of photogenerated charges and band-like transport in quantum-dot solids. *Nat. Nanotech.* **6**, 733–739 (2011).
42. Jasieniak, J., Califano, M. & Watkins, S. E. Size-dependent valence and conduction band-edge energies of semiconductor nanocrystals. *ACS Nano* **5**, 5888–5902 (2011).
43. Kwak, J. et al. Bright and efficient full-color colloidal quantum dot light-emitting diodes using an inverted device structure. *Nano Lett.* **12**, 2362–2366 (2012).
44. Pan, J. et al. Size tunable zno nanoparticles to enhance electron injection in solution processed QLEDs. *ACS Photon.* **3**, 215–222 (2016).
45. Helander, M. G. et al. Chlorinated indium tin oxide electrodes with high work function for organic device compatibility. *Science* **332**, 944–947 (2011).
46. Piprek, J., Romer, F. & Witzigmann, B. On the uncertainty of the Auger recombination coefficient extracted from InGaN/GaN light-emitting diode efficiency droop measurements. *Appl. Phys. Lett.* **106**, 101101 (2015).
47. Bae, W. K. et al. Controlled alloying of the core–shell interface in CdSe/CdS quantum dots for suppression of Auger recombination. *ACS Nano* **7**, 3411–3419 (2013).
48. Dong, Y. et al. 20.2: Ultra-bright, highly efficient, low roll-off inverted quantum-dot light emitting devices (QLEDs). *SID Symp. Dig. Tech. Pap* **46**, 270–273 (2015).
49. Fan, F. et al. Continuous-wave lasing in colloidal quantum dot solids enabled by facet-selective epitaxy. *Nature* **544**, 75–79 (2017).

Acknowledgements

This publication is based in part on work supported by the Ontario Research Fund Research Excellence Program, and by the Natural Sciences and Engineering Research Council (NSERC) of Canada. The authors thank B. Sun, M. Liu, M. Burgelman, P.-C. Li and R. Munir for their help during the course of study.

Author contributions

X.L. and F.F. conceived the idea. X.L. and F.F. developed the efficient chlorination exchange. X.L. and Y.-B.Z. fabricated and characterized the QLEDs. O.V. performed optoelectronic device simulations. L.L. and X.L. synthesized the CQDs. M.L. undertook SEM imaging. R.Q.-B. performed XPS characterizations. X.L., F.F., O.V., E.H.S. and Y.-B.Z. wrote the manuscript. O.V., E.H.S. and Z.-H.L supervised the project. All authors discussed the results and assisted in manuscript preparation.

Competing interests

The authors declare no competing interests.

Additional information

Supplementary information is available for this paper at https://doi.org/10.1038/s41566-018-0105-8.

Reprints and permissions information is available at www.nature.com/reprints.

Correspondence and requests for materials should be addressed to F.F. or O.V. or Z.-H.L. or E.H.S.

Publisher's note: Springer Nature remains neutral with regard to jurisdictional claims in published maps and institutional affiliations.

Methods

Materials. Cadmium oxide (CdO, > 99.99%), zinc acetate dihydrate ($Zn(AC)_2{\cdot}2H_2O$, 99.99%), sulfur powder (S, >99.5%), selenium powder (Se, >99.99%), oleylamine (OLA, 80–90%), octadecene (ODE, 90%), oleic acid (OA, 90%), tri-octylphosphine (TOP, 90%), thionyl chloride ($SOCl_2$), tetramethylammonium hydroxide (TMAH), 2-ethanolamine, tetrabutylammonium iodide (TBAI), tetrabutylammonium bromide (TBAB) and tetrabutylammonium chloride (TBAC), as well as all solvents used, were purchased from Sigma Aldrich without further purification.

Synthesis of the Zn–OLA complex. Under a vaccum, 2.45 g $Zn(AC)_2{\cdot}2H_2O$ was dissolved in 40 ml of OLA at 170 °C to obtain a clear solution, and then cooled to room temperature and stored in air for use.

Preparation of CdSeZnS C–S and CdSeZnS–ZnS C–S–S CQDs. The procedures for synthesis of green-emitting C–S and C–S–S CQDs were taken from the literature with some modifications[29,32]. To synthesize C–S CQDs 0.2 mmol of CdO and 4 mmol of $Zn(AC)_2$ were mixed with 5 ml of OA in a 100 ml flask and degassed for 30 min at 150 °C. Then 15 ml of ODE was injected into the reaction flask under N_2 and heated to 300 °C to get a clear solution of $Cd(OA)_2$ and $Zn(OA)_2$; 0.2 mmol of Se and 4 mmol of S dissolved in 2 ml of TOP were quickly injected into the flask at 300 °C. The reaction was kept at 300 °C for 10 min. To synthesize C–S–S CQDs the temperature of the above reaction solution was brought down to 290 °C, 1.5 ml as-prepared Zn-OLA diluted in 10.5 ml ODE was mixed with 0.03 g sulfur dissolved in 2 ml OLA, and then the mixture was injected into the flask at a speed of 14 ml h^{-1} using a syringe pump to grow the ZnS shell. After finishing injection, the solution was annealed for 10 min at 290 °C, following by an injection of 4 ml OA. The products were purified by adding acetone, centrifuging at 6,000 r.p.m. (the rotor has diameters of around 10 cm at the top and 20 cm at the bottom) and redispersing in toluene for 3 cycles.

Preparation of ZnO nanoparticles. Colloidal ZnO nanocrystals were synthesized by following a published method with some modifications[4]. $Zn(AC)_2{\cdot}2H_2O$ (3 mmol) dissolved in 30 ml of DMSO solution was mixed with 10 ml of ethanol solution containing TMAH (5.5 mmol) and stirred for 24 h under ambient conditions. ZnO nanocrystals were then precipitated by adding ethyl acetate and centrifugation at 7,000 r.p.m. for 4 min. The precipitation was redispersed in ethanol and stored in the fridge, 160 µl of 2-ethanolamine was added to stabilize the solution. The ZnO nanocrystals were further washed with ethyl acetate and redispersed in ethanol, they are filtered before use.

Device fabrication. The ITO/glass substrates were ultrasonically cleaned with deionized water, acetone and 2-propanol for 60 min, respectively. The ZnO nanoparticle solution was then spin-coated onto the ITO/glass substrates at 3,000 r.p.m. for 30 s and baked at 120 °C for 30 min. CQD dispersions in toluene (15 mg ml^{-1}) were spin-coated onto the ZnO layer at 3,000 rpm for 30 s. The film was then soaked with the $SOCl_2$/acetonitrile solution for 30 s (the volume ratio of $SOCl_2$ to acetonitrile is 1:1000, according to the calculation, the average amount of $SOCl_2$ on each CQDs is about 4.66×10^5 molecules per dot, see details in the Supplementary Information), following by two toluene rinses and subsequent baking at 120 °C for 30 min. CBP and MoO_x/Al electrodes were deposited using a thermal evaporation system through shadow masks under a high vacuum ($<10^{-4}$ Pa). The active device areas were fixed as 3.14 mm^2. All devices were measured in the air without any encapsulation.

Material characterization. Transmission electron microscopy (TEM) images were taken on a JEOL 2010, with an acceleration voltage of 200 kV. PL spectra and decay dynamics data were collected on a Horiba Flurolog time-correlated single photon counting (TCSPC) system, equipped with an iHR 320 monochromator and a PPO·900 detector. A Quanta-Phi integrating sphere was used for PLQY measurements of both the films and solutions. The morphology of the film was measured using Scan Asyst on a Bruker Catalyst in air. FT-IR spectra were obtained from a Nicolet 8700. XPS measurements were performed using a Thermo Scientific K-Alpha system with electron-gun compensation to avoid sample charging with a 50 eV pass energy and a binding energy step of 0.03–0.05 eV. The *J–L–V* characteristics of the QLEDs were measured under ambient conditions using an HP 4140B source meter. The absolute electroluminescence spectra were taken using an Ocean Optics USB4000 spectrometer that connected to a calibrated integrating sphere. An integration time of 10 ms was used for the USB4000 spectrometer to avoid saturation of the CCD (charge-coupled device). The luminance values were calculated from the absolute electroluminescence spectra assuming a Lambertian distribution of the emission profile.

Optoelectronic simulations. Calculations were carried out using the SCAPS 1D modelling suite[50]. Experimental bandgaps, band alignments, (imbalanced) mobilities, and active layer thicknesses were used (Supplementary Table 6, Fig. 3c). We note that asymmetries in the injection barriers and mobilities in the active layer can be cancelled out by adjusting the workfunctions of the respective electrodes, resulting in nearly symmetric carrier distribution profiles. The analogous adjustments are also part of experimental device optimization. For a fair comparison, simulations with low and high mobilities were optimized independently to achieve the most symmetric carrier distribution and only then compared. Simulations results are presented at biases well past the flat-band condition, but still at relatively low currents to maintain good numerical convergence. At higher injection currents, carrier imbalance and Auger recombination near the contacts will keep increasing.

Data availability. The data that support the plots within this paper and other findings of this study are available from the corresponding author upon reasonable request.

References

50. Burgelman, M., Decock, K., Khelifi, S.Abass, A. Advanced electrical simulation of thin film solar cells. *Thin Solid Film.* **535**, 296–301 (2013).